physica status solidi rrl
www.pss-rapid.com

Tetrahedral Complexity in Amorphous Networks: A Possible Clue for the Unique Properties of Phase-Change Materials

Matthieu Micoulaut,* Hugo Flores-Ruiz, Annie Pradel, and Andrea Piarristeguy

A typical binary amorphous telluride $GeTe_2$ is investigated from the first principles molecular dynamics simulations. After a comparison with chemical analogs from neutron or X-ray diffraction experiments, such as GeO_2 or $GeSe_2$, the structure of this material is focused by examining real and reciprocal space properties. It is found that the base geometrical motifs of the germanium atom can be either in tetrahedral or in defected coordinations involving pyramidal units. A review of previous results for other compositions reveals that such binary Ge tellurides contain soft tetrahedra, at variance with lighter chalcogenides, such as Ge—S and Ge—Se, and are characterized by an increased angular bending motion (typically 20°) as compared with, e.g., Ge—S (5°). In addition, for amorphous Ge-rich materials, $GeTe_2$ and GeTe, a secondary tetrahedral geometry appears, related to the presence of Ge—Ge bonds, having a larger mean angle of about 125°. These typical features not only relate to characteristics observed from scattering experiments but may also be a crucial feature for the understanding of the phase-change phenomena.

Over the past two decades, phase-change materials (PCM) have received a huge attention with various technological applications ranging from optical discs, such as DVD-RW or blue-ray discs, to phase-change memory (PC-RAM), including more recent opportunities as all-photonic memories and flexible displays with nanopixel resolution.[1] These applications build mainly on unique properties of the PCM that use the important electrical or optical contrast between a crystalline and an amorphous phase, as well as the fast recrystallization of the amorphous phase.

On PC properties and recording, special emphasis is made on short crystallization times, on the optical or electrical contrast between the amorphous and the crystalline phase,[2] on the reversibility between both phases upon a large number of phase-change cycles, and on the high thermal stability. Over the years, extensive investigations as a function of composition or alloying elements have led to the recognition that such important properties and performances are being optimized along the $GeTe - Sb_2Te_3$ join in the ternary Ge–Sb–Te system (GST). In this search for optimal performances, the key material has turned to be GeTe or $Ge_2Sb_2Te_5$, one of the very first PCM used for enhanced storage capacities[2] close to the 100GB/cm^2 domain.

Of special interest is the nature of the Ge geometry as it has been suggested that the PC mechanism is driven by switching between an octahedral (O) site in the crystalline state to a fourfold tetrahedral (T) site in the amorphous one,[3] as it is known that external conditions (light, current, and pressure) lead to an increase in the atomic bond lengths,[4,5] which appears to be one of the very obvious mechanisms able to accommodate the electronic repulsion induced by a reduction of the bond angle from 109° to about 90°. While such a simple picture might not be fully valid, a certain number of comments should be made. First, one neglects the possibility to have homopolar Ge—Ge bonds, but these are obviously present in PCM having the appropriate compositions[6] and also might drive the tendency to form T—Ge. While a certain number of contributions using density functional theory (DFT)-based simulations have found that the population of such (T) motifs represents minority sites,[7–9] it should be emphasized that the theoretical conclusions were based on electronic schemes that led to a spurious overestimation of the Ge—Te bond length, typical of octahedral geometries. In addition, the methods of estimation of the tetrahedral population η were in part inaccurate, and recently, a rigorous approach has been introduced to estimate η.[10] In parallel, improved DFT schemes (i.e., DFT-D2) using the inclusion of empirical dispersion forces have been used,[11] and these have been found to substantially improve the structural description and to reduce the Ge—Te bond length; this statement is valid for a variety of

Dr. M. Micoulaut
Physique Théorique de la Matière Condensée
Sorbonne Université
CNRS UMR
7600, Boite 121, 4 place Jussieu, 75252 Paris, Cedex 05, France
E-mail: mmi@lptl.jussieu.fr

Dr. H. Flores-Ruiz
Departamento de Ciencias Naturales y Exactas, CUValles
Universidad de Guadalajara
Carr. Guadalajara-Ameca km 45.5, Ameca, Jalisco 46600, México

Dr. A. Pradel, Dr. A. Piarristeguy
ENSCM
ICGM
Univ Montpellier
CNRS
Montpellier, France

The ORCID identification number(s) for the author(s) of this article can be found under https://doi.org/10.1002/pssr.202000490.

DOI: 10.1002/pssr.202000490

UNCORRECTED PROOF

 © 2020 Wiley-VCH GmbH

PCM in the liquid and amorphous phase.[12–15] The main outcome from these recent studies is that the structure of PC tellurides is dominated by T—Ge, a conclusion already made on different Ge—Te glasses from the simple inspection of the experimental pair correlation function, which displays similarities with one of the tetrahedral chalcogenides and a global minimum defining well-separated shells of neighbors.[16] Mössbauer spectroscopy of ^{119}Sn substituted tellurides, which probe the local geometry in amorphous tellurides, tetrahedral versus octahedral, also provides evidence that the population of T—Ge is much larger than believed from DFT-based simulations.[10,17] Can this structural picture be reconciled with the fact that only a limited degree of sp^3 hybridization must be present to enable resonance p-electron for phase switching? This question continues to be of great interest, both from the fundamental viewpoint and the applied one.

In the present contribution, we continue to explore this issue by examining the structural properties of a certain composition in the Ge—Te binary system, that is, $GeTe_2$. Our motivation is driven by the fact that this material is a chemical analog of germania or lighter chalcogenides (e.g., $GeSe_2$), which not only easily form bulk glasses but also display a fully tetrahedral network. **Figure 1** highlights the effect of Group-VI substitution on the structural properties of GeX_2 glasses (X = O, S, Se, Te) by representing the experimental total structure factor $S(k)$ accessed from neutron diffraction (ND) or X-ray diffraction (XRD), together with results from simulations. The examination of the substitution of Group-VI atoms permits one to track what aspects of structural order at short and intermediate ranges are impacted as one moves from the tetrahedral GeO_2 to the $GeTe_2$ made of probable mixed atomic geometries. To access to such information for the present telluride, we perform density functional-based simulations to extract relevant information and compare results with other compositions in the Ge—Te binary to finally establish the tetrahedral fraction η with Ge content. Results also indicate that compositions used for phase-change applications (i.e., GeTe) display tetrahedral geometries with minority populations having an angle larger than 109°, and these involve a homopolar Ge—Ge bond.

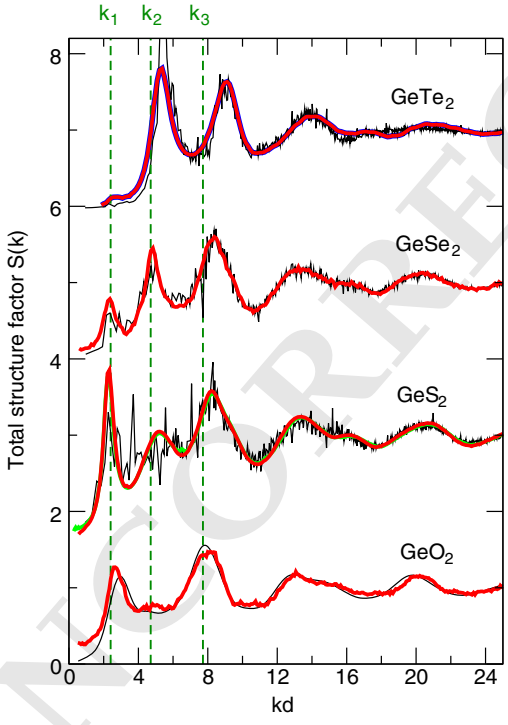


Figure 1. Total structure factor $S(k)$ for different amorphous chalcogenides rescaled as a function of kd, where d is the nearest-neighbor distance. Colored curves represent experimental data from XRD or ND, whereas thin black curves are simulation results: GeO_2[4] ($d = 1.73$Å, expt. [20]), GeS_2[23] ($d = 2.22$Å, expt.[21,51]), $GeSe_2$[24] ($d = 2.36$Å, expt.[22]), and $GeTe_2$ ($d = 2.68$Å, expt.[16]). The blue curve of $GeTe_2$ is a result from RMC simulations.[25] The broken vertical green lines represent typical positions for the first three peaks in network-forming glasses:[26] k_1, k_2, and k_3.

To assess our conclusions, we have generated a certain number of different structural models of amorphous $GeTe_2$, and these were obtained by quenching (10 K ps^{-1}) three independent configurations of equilibrated liquids obtained at 820 K, and accumulating trajectories over 30 ps each. Such liquids are supercooled given that the liquidus temperature T_L >820 K and can also be considered as equilibrated from the viewpoint of simulations, because the total energy of the system is merely constant and displays diffusive regime at large time. Note that a 920 K liquid has also been obtained and is used in the following discussion. Molecular dynamics (MD) simulations of Car–Parrinello type were performed on 200-atom systems in a cubic box with periodic boundary conditions and a density equal to experimental ones.[16] The methodology of the simulations has been given elsewhere for other compositions in the Ge—Te binary, and we refer the readers to the relevant reference for details.[10] In short, the electronic structure has been described within DFT-D2 and evolved self-consistently during the motion (time step $\Delta t = 0.12$ fs) using a generalized gradient approximation. Valence electrons were treated explicitly, in conjunction with Troullier–Martins norm-conserving pseudopotentials using a plane-wave basis set with an energy cutoff of 20 Ry. The exchange–correlation functional was taken from Perdew, Burke, and Ernzerhof (PBEsol)[18] together with the inclusion of dispersion forces[19] to improve the local structure (bond length) with respect to experimental findings.

We first represent in Figure 1 the structure factor $S(k)$ of the simulated $GeTe_2$ using

$$S_{ij}(k) = \left\langle \sum_{n=1}^{N_i} \sum_{m=1}^{N_j} e^{-ik(r_n - r_m)} \right\rangle \quad (1)$$

and

$$S(k) = \frac{\sum_{i,j} x_i x_j \alpha_i \alpha_j S_{ij(k)}}{\sum_{i,j} x_i x_j \alpha_i \alpha_j} \quad (2)$$

where x_i represents the atomic fraction of atom i, and α_i either the atomic form factor in an XRD experiment or the neutron coherence length in a neutron diffusion experiment. Equation (2) is then compared with scattering results[16] and with the results from chemical analogs of the form GeX_2 obtained either experimentally (X = O, S, Se[20–22]) or theoretically.[4,23,24]

UNCORRECTED PROOF

© 2020 Wiley-VCH GmbH

The represented materials display rather different structures as GeO_2 is entirely based on corner-sharing (CS) tetrahedra, whereas both GeS_2 and $GeSe_2$ have a mixed topology made of both CS and edge-sharing (ES) tetrahedral.[24] The structure of $GeTe_2$, albeit investigated from XRD,[16] appears to be still not fully elucidated, although reverse Monte Carlo (RMC) methods[16,25] have characterized the structure in more detail. The characterization of the local structure and environment including the degree of tetrahedral character will be discussed throughout this contribution.

There has been a recent attempt to establish ordering on typical length scales from scattering functions in tetrahedral materials,[26] and these can be summarized in a single plot (Figure 1) once the x-axis has been rescaled using the first nearest neighbor distance $d = r_{Ge-X}$ that can be determined either from the full set of calculated partial pair distribution functions $g_{ij}(r)$ or from the resolution of experimental partials using either isotopic substituted ND[20,22] or anomalous X-ray scattering (AXS[27]). Once represented as a function of kd, the structure factor features three typical peaks with positions $k_i d$ that scale as $k_1 d = 2\text{-}3$, $k_2 d = 4.6 - 4.9$, and $k_3 d = 5\pi/2 \simeq 7.7 - 8.9$ where the first one is referred to the first sharp diffraction peak (FSDP) found in a variety of glasses, and the peaks at $i = 2, 3$ are usually termed the principal peaks.

An inspection of the substitution of the progressive heavier Group-VI atoms indicates that the peak at $k_1 d$ (i.e., the FSDP) tends to vanish when moving from GeO_2 to $GeTe_2$, whereas the opposite trend is acknowledged for the peak at $k_2 d$. The peak at $k_3 d$ appears to be more or less preserved under chemical substitution, except a shift to higher kd for heavier Group-VI elements. The observed variability underscores obvious changes in the ordering of length scales.

A decomposition into partials for amorphous $GeTe_2$ (**Figure 2**) shows that the first principal peak observed at $kd \simeq 5$ (i.e., $k = 2.1 Å^{-1}$) arises essentially from all partials but with a larger contribution arising from Te—Te correlations, and the secondary principal peak having an approximate contribution of 1:2:1 from Ge—Ge, Te—Te, and Ge—Te, respectively. Note that some differences emerge from structure models obtained from RMC fits (blue curves), especially for the Ge—Ge partial, and the other two DFT calculated functions $S_{TeTe}(k)$ and $S_{GeTe}(k)$ are globally compatible with the RMC.[25]

These features rather compare well with experimental determinations from AXS for a close composition ($GeTe$[27]), and the determination of relevant partials indicates, indeed, that the principal peak at $\simeq 2 Å^{-1}$ is dominated by Te-based correlations, whereas the one at $3.5 Å^{-1}$ arises from a more equilibrated contribution from both Ge and Te.

While the peak at k_3 is found for all materials and associated with nearest-neighbor contacts that correspond to the very first shell of neighbors,[28] the second peak at k_2 is supposed to be indicative of a bonding scheme assuming directional character that leads to the formation of tetrahedral motifs.[26] This suggests that the present $GeTe_2$ is partially tetrahedral but with a Ge subnetwork that has no long-range correlation given the absence of the FSDP.

It is also instructive to inquire real-space properties, and **Figure 3**a shows the computed pair correlation functions of

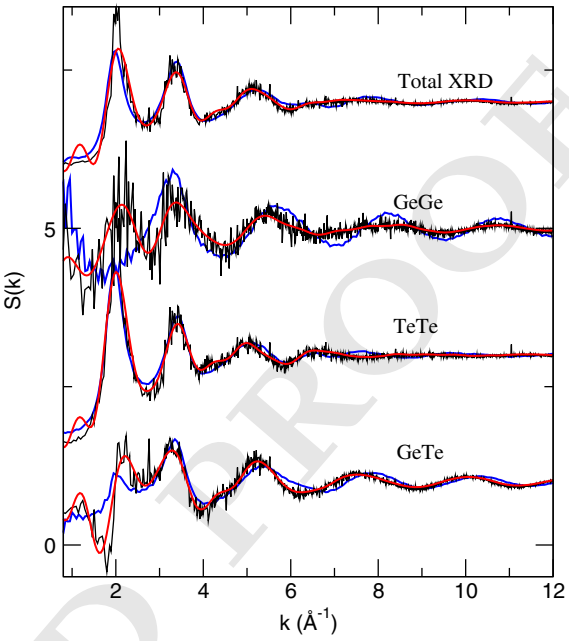


Figure 2. Calculated total structure factor $S(k)$ and Faber–Ziman-related partials $S_{ij}(k)$ of amorphous $GeTe_2$. Black curves: direct calculation from the trajectories using Equation (1). Red curves: Fourier transform of $g(r)$ and $g_{ij}(r)$. The blue curves correspond to an RMC model of $GeTe_2$.[25]

$GeTe_2$, compared with available XRD measurements from the literature.[16]

It appears that the agreement is rather very good at short distances as the main features of the pair distribution function; the main peak at 2.65 Å dominated by Ge—Te correlations (experimentally 2.61 Å[25]) is correctly reproduced, as well as the second principal peak arising from the second neighbor shell at ≃4.10 Å. This secondary peak actually results from different contributions (Ge—Te and Te—Te) and has been previously found to depend on the Ge content,[10,25] but in the present material, the Te—Te correlations essentially arise from vertices of the Ge polyhedra, and the first peak at ≃2.67 Å is associated with the remaining Te—Te homopolar bonds. Here, the structure remains, indeed, dominated by such Te—Te and Ge—Te correlations, and the possibility of having Ge—Ge atoms is still small, albeit a typical prepeak featuring the Ge—Ge homopolar bonds is found at ≃2.69 Å, i.e., somewhat larger than the corresponding distance found in $GeSe_2$ (2.44 Å[22]). The Ge—Te distance is found to increase with temperature (from 2.65 to 2.69 Å at 820 K), which is compatible with experimental studies in the liquid state,[29] albeit the bond distance is slightly underestimated with respect to experimental data (2.81 Å at 1023 K[30]). It should also be remarked that some differences with the RMC models[25] of amorphous $GeTe_2$ do appear (Figure 3b), especially for Ge—Ge and Te—Te correlations, and the amplitude of the main peak of the former is much larger than the present calculated one from DFT, which signals an increased Ge—Ge structuration for RMC structures. Similarly, the homopolar Te—Te and the Ge—Te bonds are found to be slightly smaller in RMC models. The combination of both sets of partials leads to a similar total pair

UNCORRECTED PROOF

© 2020 Wiley-VCH GmbH

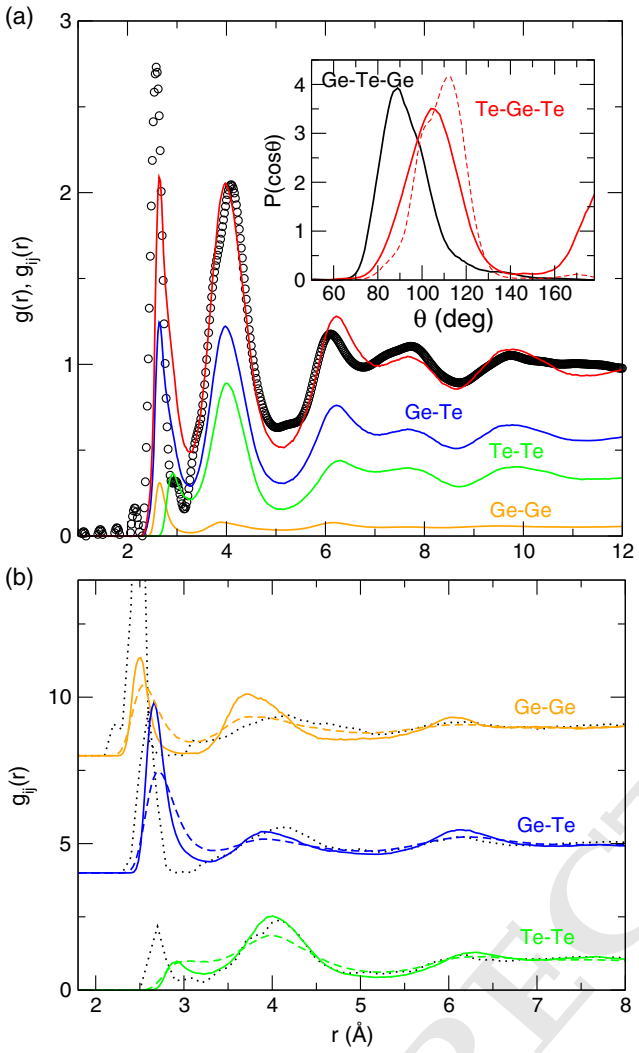


Figure 3. a) Calculated total pair correlation function $g(r)$ (red) together with corresponding weighted partials in amorphous $GeTe_2$. Experimental data from XRD are represented by circles.[25] The inset shows the calculated BADs $P(\cos\theta)$ Ge—Te—Ge (black) and Te—Ge—Te (red) together with a corresponding distribution Se—Ge—Se for $GeSe_2$ (broken red line[24]). b) Comparison of the calculated functions $g_{ij}(r)$ (solid lines, the same as panel (a)) with corresponding partials obtained in the liquid state (broken colored curves, 920 K) and from RMC (dotted lines[25]).

correlation function. The coordination numbers obtained at the minimum of the pair correlation function ($r_m = 3.27$Å) are equal to $n_{Ge} = 4.3$ and $n_{Te} = 2.7$; i.e., typical numbers found at other compositions in these Ge—Te mixtures[10,14] that underscore 1) the increased Te coordination number with respect to the octet (8-N) rule encountered in the other GeX_2 materials and 2) the increased Ge coordination number with respect to its expected value of 4 and results from a mixed population of tetrahedra and higher coordinated $n_{Ge} > 4$ defect octahedral geometries.

We now concentrate on angles. The bond angle distributions (BADs) Ge—Te—Ge and Te—Ge—Te are represented in the inset of Figure 3a and show that the Te-centered angles involve an angle of about 90°, consistently with the reported defect octahedral geometry for Te.[31] Conversely, the Ge-centered bond angle turns out to display a main distribution at 105° and a tail at 180°, which is the signature of the presence of defect octahedral geometries. Note that here, we have represented $P(\cos\theta) = P(\theta)/\sin\theta$ rather than $P(\theta)$, which permits to blow up the angles found at 180°. In fact, as the infinitesimal area element during angle calculations in spherical coordinates is $\sin\theta d\Phi d\theta$, as one approaches $\theta \to 180°$, the area goes to zero, and therefore, $P(180°) \to 0$. We also recall that the inclusion of dispersion forces tends to shift the Te—Ge—Te BAD to larger angles and to an increased tetrahedral character.[14]

To investigate the angular motion around the Ge atom, we use algorithms, which convert the bond-bending motion into a topological constraint.[32,33] Such a counting is based on partial bond angle distributions (PBADs) $P(\theta_{ij})$ that is defined from a set of neighbors. From a given trajectory, we first select N first neighbors, which lead to $N(N-1)/2$ possible angles labeled as $i0j$ with $(i,j) = \{1..N\}$ and 0 the central Ge atom; i.e., one has 102, 103, etc. From such PBADs, a corresponding first moment $\overline{\theta}$ and second moment (standard deviation) $\sigma_{\theta ij}$ can be calculated for each distribution, and this provides a measure of average angle and its excursion, which is related to the bond-bending interaction strength.[34] Such methods have permitted to estimate network rigidity in glasses and other complex materials as a function of thermodynamic conditions.[35,36] In the forthcoming, we have set $N = 6$, and this leads to 15 possible PBADs out of which different $\overline{\theta}$ and $\sigma_{\theta ij}$ (σ_θ in the forthcoming) have been calculated.

To check for the degree of rigidity of the geometrical unit, one represents $\sigma_\theta(\overline{\theta})$ for different systems. In silica where the $SiO_{4/2}$ tetrahedra are known to act as a rigid unit mode[37] and where the disordered structure of the network is achieved from a variety of angles for the bridging oxygen, such a representation leads to data found at $\overline{\theta} = 109^\circ$ only for angles $i0j$ with $i,j \leq 4$ that is also acknowledged in corresponding silicates of the form $Na_2O - SiO_2$ (SN; **Figure 4**), and such angles, furthermore, display an equivalent and low value for the corresponding standard deviation σ_θ (5°). The same behavior holds for germania (GeO_2)[34] or for window glass[38] (SCN; Figure 4).

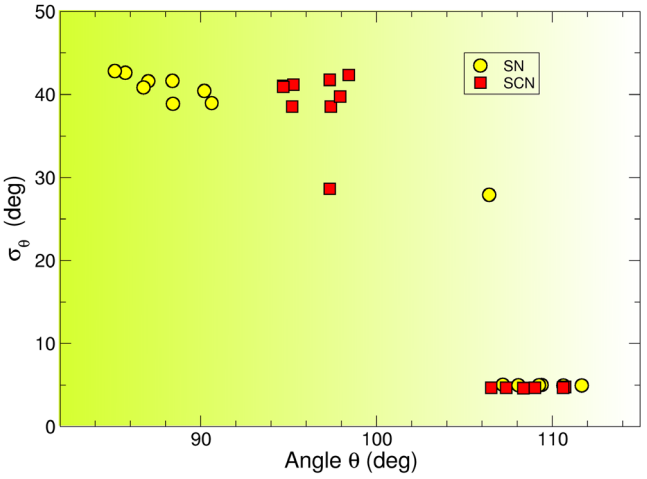


Figure 4. Plot of $\sigma_\theta(\overline{\theta})$ for the silicon atom calculated for a sodium silicate (SN[32]) and in window glass $CaO - Na_2O - SiO_2$ (SCN[38]).

UNCORRECTED PROOF

© 2020 Wiley-VCH GmbH

In contrast, angles involving atoms beyond the first shell of neighbors lead to larger bond-bending motions due to the increased distances between the central atom at the chosen (i,j) with $4 \leq i,j \leq N$. This leads to a broad distribution for the corresponding average angle $\overline{\theta}$, which is found in the range between $90° \leq \overline{\theta} \leq 105°$. Such angles are, furthermore, characterized by a large angular standard deviation ($\sigma_\theta \simeq 40°$) and are not considered here, given that they do not contribute to the characterization of the short-range order.

Figure 5 now represents the same quantity for binary germanium chalcogenides Ge-X with changing composition (X = S, Se, Te). Noticeable features can be detected in the region of interest ($\overline{\theta} \simeq 109°$, $\sigma_\theta \simeq 8-20°$). Germanium sulfides[23] exhibit a similar trend to the one determined for the oxides; i.e., whatever the considered composition smaller than the stoichiometric GeS_2 (Ge_xS_{100-x}, $x \leq 1/3$), the $GeS_{4/2}$ tetrahedra appear to be well defined and rigid because of a low value for the angular excursion ($\sigma_\theta \simeq 8°$) that is sharply centered around $\overline{\theta} \simeq 109°$. An almost similar situation is encountered in Ge_xSe_{100-x} selenides, and here also, σ_θ appears to be low for the angles defining the Ge tetrahedron, except for compositions satisfying $x \geq 33.3\%$ (not shown here). Here, it was found that the part of the increasing stress imposed by Ge additional cross-links can be released by softening of the angular constraints, which manifests by an increased bending motion inside the tetrahedra[24] as also detected in the liquid phase when thermal activation softens bending interactions.[23]

The situation is dramatically changed in Ge—Te binary alloys. A representation for various compounds recently investigated[10,14] including the present $GeTe_2$ indicates that angles around the Ge atoms experience wider angular motions, and this increases σ_θ to about $15-20°$ indicative of soft geometrical unit at variance with the rigid unit mode encountered in silicas.[37]

A representation of different PCM previously investigated[39] can be plotted to provide some perspective (**Figure 6**). It is seen that PCM (e.g., $Ge_1Sb_2Te_4$ [GST124]) are characterized by large angular excursions ($10°-25°$) and angles that are somewhat smaller than the tetrahedral value but are larger than the typical value of pyramidal geometries (98°) typical of Group-V elements, such as As_2Se_3. For the tellurides, it is, furthermore, seen that as averages are performed over the whole system, angles $\overline{\theta}$ (i.e., first moments of the PBADs) involving the first four neighbors of the Ge atom span between the two limiting values of 98° and 109°.

Using such angular constraints, a recent method permits to rigorously extract the fraction of Ge tetrahedra.[10] The detection and quantification of tetrahedral germanium can be made from the previously introduced method but instead of ensemble averaging to obtain, e.g., Figure 5, one performs a selection of individual Ge atoms with a rule based on angular standard deviations. This has the advantage to focus on angular excursions only, rather than working directly on angles, which span over a restricted domain. Angles are followed individually during the simulation from the $N(N-1)/2$ possible triplets i-Ge-j defined by a set (i,j) of N first neighbors. If the calculated number of low standard deviations around such atoms is six, a tetrahedron is identified, because this geometry is defined by six rigid

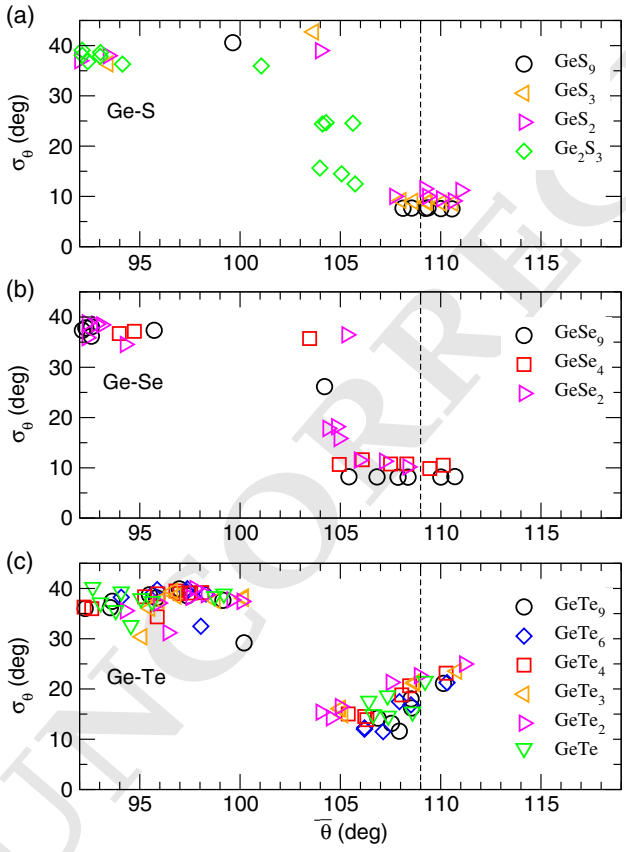


Figure 5. Measure of the Ge angular excursion $\sigma_\theta(\bar{\theta})$ in binary Ge-X chalcogenides. a) X = S from simulations published in the previous study.[23] b) X = Se from the previous study[24] and c) X = Te from the previous studies[10,14] and the present work. The broken vertical line represents the value of the tetrahedral angle.

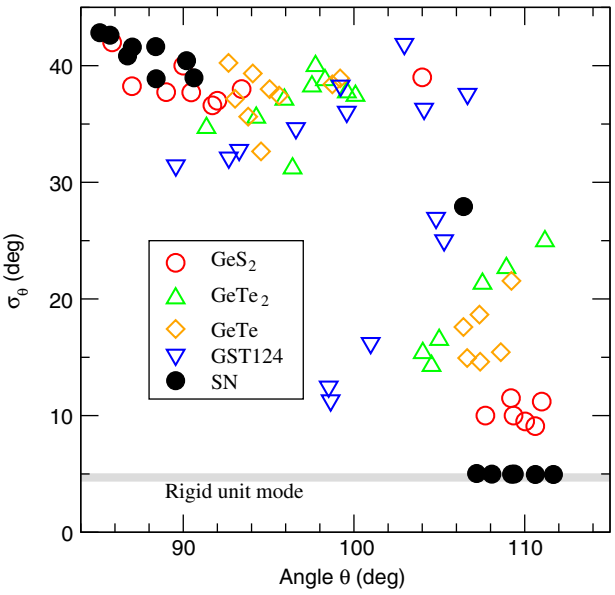


Figure 6. Comparison of the Ge angular excursion $\sigma_\theta(\theta)$ in different phase-change alloys, compared with reference materials (SN, the same as in Figure 4).

UNCORRECTED PROOF

© 2020 Wiley-VCH GmbH

angles that give rise to corresponding low standard deviations with associated angles that are all close to 109°.

Averages over the entire system for such identified Ge atoms then lead to a BAD that has the property of having six rigid angles and centered around 109° (black curve, **Figure 7**).

This distribution for $GeTe_2$ is centered at an angle that is exactly equal to the tetrahedral angle as already acknowledged for GeTe.[14] Interestingly, the (T) distribution exhibits a tail at large θ that is not obtained in the corresponding selenide glass,[24] and it signals that tetrahedral Ge atoms display two distinct populations in this $GeTe_2$ material as the six constrained angles can also experience angular excursions that are larger than the average 109°, i.e., in the domain between $120° \leq \theta \leq 160°$.

The residual distribution (nT) has the following properties (red curve, Figure 7). It is centered at $\overline{\theta} \simeq 98°$, i.e., typical of a pyramid with a triangular basis having the Te—Te bonds as edges, and a Ge at the remaining vertex, similar to the pyramidal geometry found in As_2Se_3 for which three rigid angles are obtained.[33] In the present $GeTe_2$, similar findings are obtained, and the (nT) is, indeed, also characterized by three rigid angles with $\sigma_{\theta ij} \simeq 15°$. Note that possible additional longer bonds do exist, but these do not constrain the geometry as they involve $\sigma_{\theta ij} \simeq 30° - 40°$.

Finally, the fraction η of tetrahedral Ge can be calculated from the number of atoms fulfilling six standard deviations with a low value, and for the present $GeTe_2$, we find $\eta = 55.0 \pm 1.0$ in amorphous phase. This value is similar to numbers previously found at close compositions ($GeTe_4$, $\eta = 54.6\%$[10]).

The results obtained for $GeTe_2$ are now put in perspective with previous ones obtained for other compositions in this Ge—Te binary.

Figure 8 represents the obtained evolution of the tetrahedral population in Ge_xTe_{100-x} as a function of Ge content x. It shows that chalcogen-rich and Ge-rich materials contain a large amount of tetrahedral Ge, of about 60–65%. At large Ge content, the enhancement of the (T) population is known to be driven by the presence of homopolar bonds, which lead to energetically more favorable structures in (T) geometry,[6] whereas the increased presence of such motifs at low x seems compatible

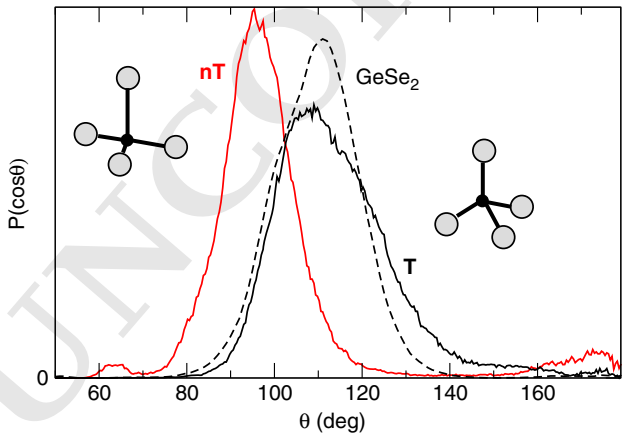


Figure 7. BAD of identified tetrahedral (T, black) and non-tetrahedral (nT, red) Ge in $GeTe_2$. Associated structures are represented. The broken curve corresponds to the Se—Ge—Se BAD in the isochemical $GeSe_2$.[24]

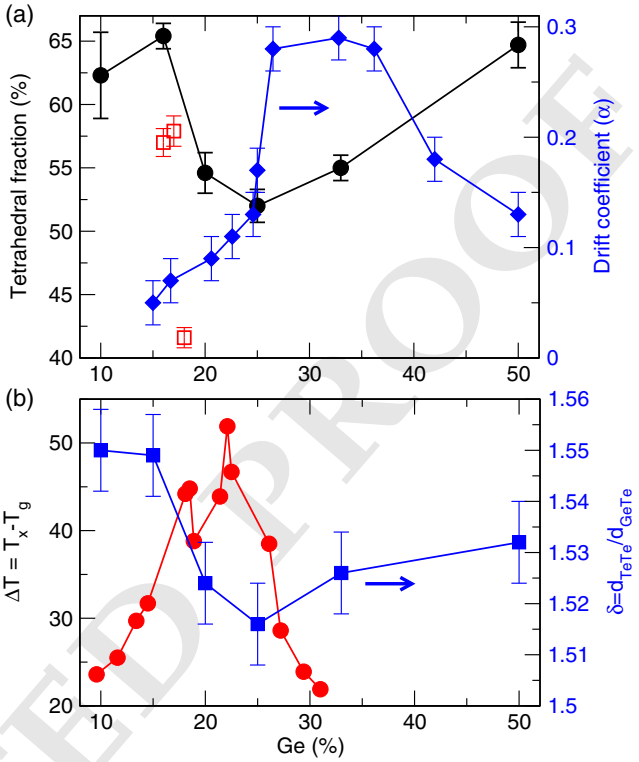


Figure 8. a) Evolution of the calculated tetrahedral fraction $\eta(x)$ as a function of Ge content in amorphous Ge_xTe_{100-x} systems (see the previous studies,[10,14] and the present work). The red open symbols represent experimental numbers extracted from Mössbauer spectroscopy.[10] Right axis: Experimentally drift coefficient characterizing the time evolution (aging) of the resistivity (blue symbols).[42] b) Thermal stability $\Delta T = T_x - T_g$ in Ge_xTe_{100-x}, measured by differential scanning calorimetry.[16] Right axis: Calculated ratio $\delta = d_{TeTe}/d_{GeTe}$ as a function of Ge content (blue symbols).

with an measurement from Mössbauer spectroscopy. This experimental technique finds a (T) fraction η of about 57% around the eutectic composition $Ge_{15}Te_{85}$, prior to an important decrease close to $GeTe_4$ (41.6±0.8[10]), which indicates that Ge atoms are then predominantly found in an octahedral geometry. While this fraction is not fully reproduced from our simulations, we do find that $\eta(x)$ displays a minimum value for larger Ge content, close to the $GeTe_3$ composition (52%), and the structure of GeTe is dominated by tetrahedra ($\eta = 64.7\%$). It is important to emphasize at this stage that the chosen electronic schemes alter dramatically the calculated value of η and DFT calculations, which do not consider a dispersion correction lead to values that are much lower ($\eta = 41.2\%$[14]), a result that is directly driven by increased (i.e., overestimated) Ge—Te bond lengths, which promote octahedral geometries.

An indirect evidence for the evolution of (T) population with Ge content is also provided by the ratio $\delta = d_{TeTe}/d_{GeTe}$ that is calculated from the relevant partial pair correlation functions. This ratio usually serves to characterize the modification in tetrahedral bonding,[4] given that for perfect tetrahedral geometries, one can expect to have the ratio δ_X of the vertex distance d_{XX} over the Ge-X distance d_{GeX} (X = O, S, Se) to be:

UNCORRECTED PROOF

© 2020 Wiley-VCH GmbH

$\delta = d_{XX}/d_{GeX} = \sqrt{8/3} = 1.63$, which is fulfilled in tetrahedral selenides and sulfides,[26] whereas the same ratio in a perfect octahedral bonding is given by $\delta = \sqrt{2} = 1.41$. The departure from the value $\sqrt{8/3}$, thus, signals for certain systems a tetrahedral to octahedral conversion.[4] In the present tellurides, it is seen that δ is found between the limiting values of 1.41 and 1.63 (Figure 8b, right axis), which signals, indeed, that the Ge is found as a mixture of (T) and (O) populations. Interestingly, the minimum evolution of η with Ge content correlates directly with the one found for δ, and the latter is essentially driven by a reduction in the domain ≃20–35% Ge of the Te—Te bond distance defining the vertex of the polyhedra. An alternative means of analyzing the tetrahedral fraction is the consideration of the single Ge—Te bond length d_{GeTe}.[27] In the present tellurides, the change with composition is too small and appears to be weakly sensitive to Ge content as d_{GeTe} is always found between 2.63(9) and 2.65(4) Å.

Figure 9 represents the different obtained Ge-centered BADs fulfilling six rigid angles. All are, indeed, centered around 109°, although one notices increased excursions at large θ for the $GeTe_2$ and GeTe compositions. A convenient way to provide an increased characterization of the effect of composition is to interpret the BADs in terms of an effective potential $U_{eff}(\theta)$, assuming that one has

$$P(\cos\theta) \propto \exp[U_{eff}(\theta)/k_B T] \quad (3)$$

as introduced in studies on liquid–liquid transitions of silica.[40] We, furthermore, assume that the effective potential is harmonic with a compositional-dependent stiffness constant k_2, i.e., $U_{eff}(\theta) = \frac{1}{2}k_2(x)(\theta - \theta_0)^2$, and θ_0 being the tetrahedral angle. Using Equation (3), we fit the represented BADs and extract a stiffness k_2 that is now represented as a function of Ge content (Figure 9). Note that θ_0 is left as an adjustable parameter, and the fits lead systematically to the values in the range $110.0° - 112.3°$, except for two compositions ($GeTe_2$ and GeTe), which needed an additional distribution of the form of Equation (3) because of the presence of a tail in the BAD at $\theta \simeq 130° - 140°$. This second contribution involves an additional fitted mean angle obtained at $\theta_0 = 124.9°$ for GeTe (115.2° for $GeTe_2$) and smaller stiffness k_2. The detailed analysis of the Ge-centered BADs shows that this contribution is associated with a Ge—Ge—Te BAD, and the emergence of such motifs is linked with the growing presence of homopolar bonds that have been detected from RMC simulations once $x > 20\%$.[25] The evolution of k_2 for the main contribution (i.e., at 109°) with Ge content is compatible with the trend observed for the tetrahedral fraction (Figure 8) as large k_2 values imply that more tetrahedra are present in the structure with small harmonic excursions away from 109°. The stiffness appears, however, to be much smaller than the one calculated from a trajectory of $GeSe_4$[24] where a similar fit on the Se—Ge—Se BAD leads to $k_2 = 315.7\,J\,mol^{-1}\,deg^{-1}$, i.e., much larger than for the corresponding tellurides, and this selenide material is, indeed, made of 100% tetrahedra.

The presence of a minimum in tetrahedral fraction (Figure 8) and stiffness k_2 in this compositional range (20–33%) has a link with a possible flexible to rigid transition but with features that

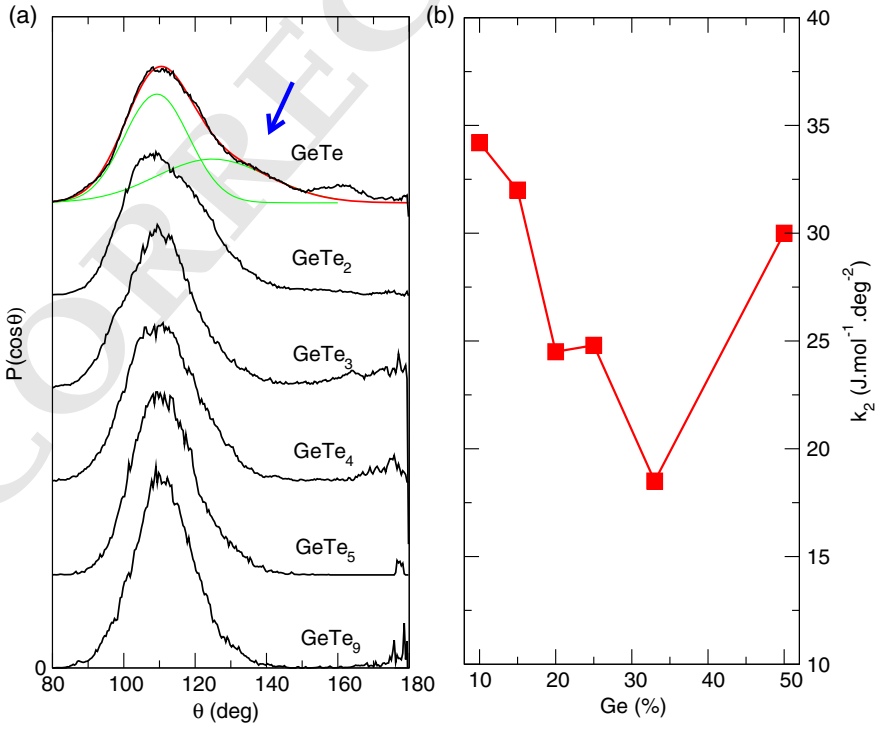


Figure 9. a) Calculated Ge-centered BADs $P(\cos\theta)$ fulfilling six rigid angles for different compositions in Ge—Te binary. The thin red line represents a fit using Equation (3) over the $80° - 150°$ angular domain for GeTe, and green curves correspond to the two respective contributions centered at 109.2° and 124.9° (see text for details). b) Fitted stiffness k_2 at ≃ 109° for the Ge-centered bond angle as a function of Ge content x in amorphous Ge_xTe_{100-x}.

UNCORRECTED PROOF

© 2020 Wiley-VCH GmbH

turn out to be specific to tellurides, given that the fraction of tetrahedra evolves with Ge content. Such transitions are being currently observed for the other chalcogenides, e.g., Ge_xSe_{100-x}[24] or Ge_xS_{100-x}.[23] At this transition, a certain number of physicochemical properties display minima or maxima, and for selenides or sulfides, this transition point is located at $x_c = 20\%$.[33] While this transition point at x_c can be predicted exactly from a mean-field treatment of radial and angular rigidity in such lighter chalcogenides where the octet rule applies, the uncertainties associated with the increased electronic delocalization of the bonding make the application of such theoretical methods more problematic in tellurides.

An inspection of Figure 8 indicates that the anomaly observed for η correlates with properties measured in the context of phase-change applications.

The evolution of the drift of the resistivity with Ge content appears to be related to the change in local geometry. This drift is usually described by a power law of the form $\rho(t)/\rho_0 = (t/t_0)^{\alpha}$, where ρ_0 is the resistivity at the initial time t_0, the exponent α characterizing the behavior with time.[41] Once represented as a function of Ge content (Figure 8a, right axis), one realizes qualitatively that PCM with a large amount of (T) geometries will display a smaller variation in resistivity (small α values), and the abrupt change in $\alpha(x)$ at $x_c = 23\%$ is possibly related to a flexible to rigid transition.[42] The important increase in the drift coefficient resistivity at this rigidity threshold obviously reflects a higher tendency to aging for Ge-rich layers, and is also associated with the appearance of the homopolar Ge—Ge bonds.[25,43]

Figure 8b also shows some correlation with the fraction of tetrahedra, and one acknowledges an enhanced thermal stability $\Delta T = T_x\text{-}T_g$ close to 22% Ge. Here, T_x is the temperature of crystallization onset, and T_g is the glass-transition temperature,[16] which reflects the ability of the material to vitrify, and ΔT is maximum in the region where the population of both tetrahedra and defect octahedra is about the same.

Regarding the link between PC phenomena and local structure/geometry, the picture that emerges from our analysis is the following. At large Ge content, apart (O) local geometries, (T) display two types of short range order: a first one that is, indeed, close to the value $\arccos(-\frac{1}{3}) = 109.47°$ and dominant at small composition x (Figure 9) where the effects of stress and presence of homopolar Ge—Ge bonds is negligible. With increasing Ge content, the rigidity induced from increased stress/bond density[33] is partially released by a global reduction of the (T) fraction to about ≃50% at $GeTe_3$ (Figure 8a) as less angular rigid constraints are involved, because these evolve as $5\eta + 3(1\text{-}\eta) = 3 + 2\eta$.[17] For larger concentration, the emergence of Ge—Ge bonds promotes back again (T) geometries,[6] and a second (T) contribution emerges at $115 - 124°$ that involves a homopolar bond and continues to have six rigid angles. It is already detected for $GeTe_2$ (Figure 9). The deviation from a standard tetrahedral angle to larger values is rather well known in the literature and found in strained molecules, such as, e.g., fenestranes,[44] a class of materials where the bond lengths deviate from those found in reference alkanes and induce a bond angle at the central carbon atom of around 130°. The mechanism of "planarization" of the tetrahedral carbon results of a gradual increase in bond angle deformation and strain energy that effect a change in hybridization.[45] In the present tellurides, this secondary (T) population appears to be an intermediate geometry between the regular (T) and the (O) geometry, promoted by the presence of stress.

The fact that the intratetrahedral bending motion is more soft in tellurides must have some implications for corresponding vibrational spectra as acknowledged, e.g., for the case of densified silicas.[46] In Ge—Te glasses,[42] the Raman spectra contain features of Te-sites but also signatures of Ge-based local geometries with typical frequencies of $122 - 126$ and $160\,cm^{-1}$ for defect octahedra and a broadband centered around $190\,cm^{-1}$ for tetrahedral.[47] Using an effective mass m for the vibrating structures (i.e., corresponding to the chalcogen mass, which is larger in the case of Te-based glasses), one can estimate the typical frequency of bending modes $\omega_{BB} = \sqrt{\beta/m}\cos\theta/2$ from a nearest-neighbor central-force model.[48] It indicates that ω_{BB} must be smaller in tellurides as the restoring force constant β must be lower in $GeTe_\gamma$ due to the increased angular excursion, when compared with, e.g., selenides, which involve an increased frequency for bending motion[49] as also acknowledged for vibrational study of S/Se substitution in stoichiometric compounds.[50]

In the present contribution, DFT-based simulations, we have focused on the structure of $GeTe_2$, an isochemical compound of tetrahedral network formers of the form GeX_2 (X = O, S, Se). These simulations appear to reproduce rather accurately the overall structural properties of the amorphous phase, as acknowledged by a rather good agreement with experimental structure functions (structure factor $S(k)$ and pair correlation functions $g(r)$). We have then focused on the geometrical motif associated with Ge atoms and results that indicate a rather important fraction of tetrahedra (55%), but these appear to be soft units that experience angular excursions up to $160° - 170°$ during bond-bending motions. These excursions are larger than in corresponding sulfides and selenides whose short range order can be fairly described within a rigid unit model typical of oxide network formers (GeO_2, SiO_2).

Once the fraction of tetrahedra is followed as a function of Ge content, a minimum is obtained close to a reported rigidity transition, whereas Ge-rich compositions and GeTe appear to contain the largest population of tetrahedra but, in the last case, with a secondary geometry, related to the presence of Ge—Ge bonds, having a mean angle of about 125° that leads to a specific tail in the BAD at large angles. These trends permit to decode observed anomalies in properties regarding phase-change mechanisms, and might be of some interest for further work in terms of applications. More generally, the ease of phase switching is directly linked to small ionicity and a limited degree of hybridization, enabling some resonance p-electron bonding to prevail. This means that sp^3 tetrahedral geometries involving occupied but energetically unfavorable sp^3 antibonding states might lead to the absence of resonance bonding. The fact that such (T) units appear to be much softer than their selenide or sulfide counterparts, able to explore larger angles and possible additional interactions, indicates that even tetrahedral tellurides can be promising candidates for PC applications.

UNCORRECTED PROOF

© 2020 Wiley-VCH GmbH

Acknowledgements

The authors acknowledge support from Agence Nationale de la Recherche (ANR) (Grant No. ANR-11-BS08-0012).

Conflict of Interest

The authors declare no conflict of interest.

Keywords

ab initio simulation, bond angle distribution, geometrical motifs, phase-change materials

Received: October 14, 2020
Revised: November 6, 2020
Published online:

[1] W. Zhang, R. Mazzarello, M. Wuttig, E. Ma, *Nature Rev. Mat.* **2019**, *4*, 150.
[2] *Phase Change Materials And Applications*, (Eds: S. Raoux, M. Wuttig), Springer, Berlin **2008**.
[3] A. V. Kolobov, P. Fons, A. I. Frenkel, A. L. Ankudinov, J. Tominaga, T. Uruga, *Nat. Mater.* **2004**, *3*, 703.
[4] M. Micoulaut, *J. Phys.: Condens. Matter* **2004**, *16*, L131.
[5] D. A. Baker, M. A. Paesler, G. Lucovsky, S. C. Agarwal, P. C. Taylor, *Phys. Rev. Lett.* **2006**, *96*, 255501.
[6] J.-Y. Raty, W. Zhang, J. Luckas, C. Chen, R. Mazzarello, C. Bichara, M. Wuttig, *Nat Commun* **2015**, *6*, 7467.
[7] J. Akola, R. O. Jones, *Phys. Rev. Lett.* **2008**, *100*, 205502.
[8] S. Gabardi, S. Caravati, G. C. Sosso, J. Behler, M. Bernasconi, *Phys. Rev. B* **2015**, *92*, 054201.
[9] S. Caravati, M. Bernasconi, M. Parrinello, *J. Phys.: Condens. Matter* **2010**, *22*, 315801.
[10] M. Micoulaut, K. Gunasekera, S. Ravindren, P. Boolchand, *Phys. Rev. B* **2014**, *90*, 094207.
[11] M. Micoulaut, *J. Chem. Phys.* **2013**, *138*, 061103.
[12] M. Micoulaut, M.-V. Coulet, A. Piarristeguy, M. R. Johnson, G. J. Cuello, C. Bichara, J.-Y. Raty, H. Flores-Ruiz, A. Pradel, *Phys. Rev. B* **2014**, *89*, 174205.
[13] H. Flores-Ruiz, M. Micoulaut, M.-V. Coulet, A. A. Piarristeguy, M. R. Johnson, G. J. Cuello, A. Pradel, *Phys. Rev. B* **2015**, *92*, 134205.
[14] M. Micoulaut, A. Piarristeguy, H. Flores-Ruiz, A. Pradel, *Physical Review B* **2017**, *96*, 184204.
[15] A. Bouzid, C. Massobrio, M. Boero, G. Ori, K. Sykina, E. Furet, *Phys.Rev. B* **2015**, *92*, 134208.
[16] P. **Jóvári**, A. Piarristeguy, R. Escalier, I. Kaban, J. Bednarcik, A. Pradel, *J. Phys. Condens. Matter* **2013**, *25*, 195401.
[17] K. Gunasekera, P. Boolchand, M. Micoulaut, *J. Appl. Phys.* **2014**, *115*, 164905.
[18] J. Akola, R. O. Jones, S. Kohara, T. Usuki, E. Bychkov, *Phys. Rev. B* **2010**, *81*, 094202.
[19] S. Grimme, *J. Comput. Chem.* **2006**, *27*, 1787.
[20] P. S. Salmon, A. C. Barnes, R. A. Martin, G. J. Cuello, *J. Phys.: Condens. Matter* **2007**, *19*, 415110.
[21] A. Bytchkov, C. J. Cuello, S. Kohara, C. J. Benmore, D. L. Price, E. Bychkov, *Phys. Chem. Chem. Phys.* **2013**, *15*, 8487.
[22] P. S. Salmon, J. Non-Cryst, *Solids* **2007**, *353*, 2959.
[23] S. Chakraborty, P. Boolchand, M. Micoulaut, *Phys. Rev. B* **2017**, *96*, 094205.
[24] M. Micoulaut, A. Kachmar, M. Bauchy, S. Le Roux, C. Massobrio, M. Boero, *Phys. Rev. B* **2013**, *88*, 054203.
[25] A. Piarristeguy, M. Micoulaut, R. Escalier, P. Jóvári, I. Kaban, J. van Eijk, J. Luckas, S. Ravindren, P. Boolchand, A. Pradel, *J. Chem. Phys.* **2015**, *143*, 074502.
[26] P. S. Salmon, A. Zeidler, *J. Stat. Mech.* **2019**, 114006.
[27] J. R. Stellhorn, S. Hosokawa, W.-C. Pilgrim, N. Blanc, N. Boudet, H. Tajiri, S. Kohara, *Phys. Status Solidi* **2016**, *253*, 1038.
[28] M. Micoulaut, *J. Phys. Condens. Matter.* **2019**, *31*, 285402.
[29] S. Hosokawa, K. Tamura, M. Inui, H. Endo, *J. Non-Cryst. Solids* **1993**, *156–158*, 712.
[30] I. Kaban, P. **Jóvári**, W. Hoyer, R. G. Delaplane, A. Wannberg, *J. Phys. Cond. Matt.* **1993**, *18*, 2749.
[31] J. Akola, R. O. Jones, *Phys. Rev. B* **2007**, *76*, 235201.
[32] M. Bauchy, M. Micoulaut, *J. Non-Cryst. Solids* **2011**, *357*, 2530.
[33] M. Micoulaut, *Adv. Physics X* **2016**, *1*, 147.
[34] M. Bauchy, M. Micoulaut, M. Celino, M. Boero, S. Le Roux, C. Massobrio, *Phys.Rev.B* **2011**, *84*, 054201.
[35] M. Bauchy, M. Micoulaut, M. Boero, C. Massobrio, *Phys. Rev. Lett.* **2013**, *110*, 165501.
[36] M. Bauchy, M. J. Abdolhosseini Qomi, C. Bichara, F.-J. Ulm, R. J.-M. Pellenq, *J. Phys. Chem. C* **2014**, *118*, 12485.
[37] M. Dove, K. Hammonds, M. Harris, V. Heine, *Mineral. Mag.* **2000**, *64*, 377.
[38] O. Laurent, B. Mantisi, M. Micoulaut, *J. Phys. Chem. B* **2014**, *118*, 12750.
[39] M. Micoulaut, C. Otjacques, J.-Y. Raty, C. Bichara, *Phys. Rev. B* **2010**, *81*, 174206.
[40] E. Lascaris, M. Hemmati, S. V. Buldyrev, H. E. Stanley, C. A. Angell, *J. Chem. Phys.* **2014**, *140*, 224502.
[41] M. Boniardi, A. Redaelli, A. Pirovano, I. Tortorelli, F. Pellizzer, *J. Appl. Phys.* **2009**, *105*, 084506.
[42] J. Luckas, A. Olk, P. Jost, H. Volker, J. Alvarez, A. Jaffré, P. Zalden, A. Piarristeguy, A. Pradel, C. Longeaud, M. Wuttig, *Appl. Phys. Lett.* **2014**, *105*, 092108.
[43] A. V. Kolobov, P. Fons, J. Tominaga, *Phys. Rev. B* **2013**, *87*, 155204.
[44] V. B. Rao, C. F. George, S. Wolff, W. C. Agosta, J. Am, *Chem. Soc.* **1985**, *107*, 573.
[45] R. Keese, *Chem. Rev.* **2006**, *106*, 4787.
[46] B. Hehlen, *J. Phys. Cond. Matt.* **2010**, *22*, 022401.
[47] R. Mazzarello, S. Caravati, S. Angioletti-Uberti, M. Bernasconi, M. Parrinello, *Phys. Rev. Lett.* **2010**, *104*, 085503.
[48] P. N. Sen, M. F. Thorpe, *Phys. Rev. B* **1977**, *15*, 4030.
[49] P. Boolchand, W. J. Bresser, *Phil. Mag.* **2000**, *80*, 1757.
[50] X. Han, H. Tao, L. Gong, X. Wang, X. Zhao, Y. Yue, J. Non-Cryst, *Solids* **2014**, *391*, 117.
[51] A. Zeidler, W. E. Drewitt, P. S. Salmon, A. C. Barnes, W. A. Crichton, S. Klotz, H. E. Fischer, C. J. Benmore, S. Ramos, A. C. Hannon, *J. Phys.: Condens. Matter* **2006**, *21*, 474217.

UNCORRECTED PROOF

 © 2020 Wiley-VCH GmbH